ASIA-PACIFIC SOLAR RESEARCH CONFERENCE

PEER REVIEWED
ASIA-PACIFIC
SOLAR RESEARCH CONFERENCE

Daniel Potter

Simulation of a demonstration high temperature liquid sodium receiver with Heliosim

D. Potter[1], J.-S. Kim[1] and R. McNaughton[1]

[1]*CSIRO Energy, PO Box 330, Newcastle, NSW 2300, Australia*
E-mail: daniel.potter@csiro.au

Abstract

Simulations using CSIRO's Heliosim software have been performed to estimate the performance of a conceptual design for a 700 kW_{th} high temperature sodium receiver. Comparisons were made between a simple model where pipe modules are approximated as flat surfaces, and a detailed model where the actual cylindrical geometry of each heat transfer pipe was retained. Although the simple model was found to reproduce the thermal output of the detailed model with an error of 0.5% and require over an order of magnitude less wall time and memory, the net flux through the pipe wall was underpredicted by up to 7 %. The results demonstrate the importance of considering the actual cylindrical geometry of heat transfer pipes when designing a receiver where the incident solar radiation is not normal to the pipe crown.

1. Introduction

As part of the Integrated Test Facility program of ASTRI, a high temperature liquid sodium loop with an on-sun receiver is to be installed and operated at the CSIRO's 'Solar Field 2' experimental concentrated solar thermal (CST) facility in Newcastle. ANU and the CSIRO are developing a number of conceptual designs for the demonstration receiver, one of which will be selected for fabrication, installation and operation in 2020. The demonstration receiver will have sodium inlet and outlet temperatures of 520 and 740 °C, respectively, and a nominal thermal capacity of 700 kW/m^2.

The utilisation of liquid sodium as a heat transfer fluid (HTF) in tubular receivers is of interest due to its excellent heat conduction properties and liquid state over the relatively wide temperature range of 98 to 890 °C (Romero and González-Aguilar, 2017). Although sodium as a HTF for CST applications has been investigated in numerous studies from 1980's to the present (Schiel and Geyer, 1988; Boerema et al., 2012), the focus has largely been on the lower temperature ranges relevant to subcritical steam turbines ($\approx$ 290 to 560 °C). In this work, higher inlet and outlet temperatures suitable for interfacing with high efficiency power cycles such as supercritical CO_2 Brayton cycles (Padilla et al., 2015) are being considered. This high operating temperature range brings additional challenges to the receiver design, due to the increased potential for thermal loss and reduced material strength of pipe materials.

In previous work by the authors, an integrated computational model for optical and thermal analysis of central receiver CST systems was applied to optimise the field layout and receiver geometry for a 1 MW_{th} liquid sodium cavity receiver (Potter et al., 2015). The receiver was a PS10-like design with four pipe modules (arrays of heat transfer pipes running parallel to each other and connected by headers) contained within a cavity with a 82.5 cm diameter circular aperture. The receiver was mounted on a tower to be 30 m above ground level, and the whole

receiver rotated 60° down towards the heliostat field. The pipe modules were approximated as flat surfaces in the computational model, and the design point receiver efficiency of the optimised design was calculated to be 91.7%.

The present work utilises a significantly improved version of the above mentioned integrated computational model to evaluate the performance of the CSIRO 'Mark I' design for the demonstration receiver. The integrated computational model has since been developed into a multi-platform computer software package called Heliosim (Potter et al., 2018) with numerous improvements to both the physical modelling and user interface. The improvements to the physical modelling relevant to the present work are the implementation and validation of a Monte Carlo ray tracing model (Wang et al., 2018), and the implementation of a detailed heat transfer model where the actual cylindrical geometry of individual pipes is considered when performing both optical and heat transfer simulations of receivers.

Although Heliosim was also a key tool used in designing the receiver, the focus of the present work is the simulation of the receiver performance. In particular, comparisons are made between simplified and detailed representations of the receiver geometry. The simplified geometric representation approximates the pipe modules as flat surfaces, whilst the detailed representation retains the actual geometry of each cylindrical pipe and the backing insulation. The detailed model allows the circumferential distribution of flux, temperature and stress for each pipe to be investigated. The comparison between these two models is of interest as the simple model requires significantly less computational resources and is suitable for incorporation into an objective function for the coupled optimisation of the heliostat field and receiver design for commercial facilities. The simplified model, however, makes a number of approximations (e.g. rear half of pipes are adiabatic, and incident radiation is perpendicular to the pipe modules) that may not be appropriate for all receiver geometries. By comparing the detailed and simple models, the validity of these approximations can be investigated.

In § 2 and § 3, respectively, the CSIRO 'Solar Field 2' facility and 'Mark I' sodium receiver design are described. An overview of the relevant physical modelling implemented in the Heliosim software is given in § 4. Results and discussion of the performance evaluation simulations are presented in § 5 and § 6, respectively, and conclusions are made in § 7.

2. Experimental facility

The demonstration receiver is being designed for operation at the 'Solar Field 2' facility at CSIRO Newcastle. The key parameters describing the solar collection and concentration system are provided in Table 1. The solar collection and concentration system consists of 396 single facet heliostats with tilt-roll actuation, and can deliver up to 1.5MW of radiative power at the focal point[1]. The heliostats utilise the CSIRO's patented low cost heliostat construction methods and design (Burton and Andrews, 2011). Five facet focal length variants are installed; the seating plan of these facets is presented in Figure 1. The nominal facet slope error and tracking error are conservative estimations based on analysis of historical calibration target images. Due to the planned installation of a falling particle receiver at the center of the tower platform, the likely location of the sodium receiver aperture is offset approximately 2.7 m from the nominal focal point of the facility.

[1] Approximately 1.5 MW can be intercepted at the summer solstice by a 1m radius circular target with -45° elevation angle and a DNI of 1000 W/m^2.

Parameter	Value
Count	396
Actuation	Tilt-roll
Facet width × height (m)	1.85 × 2.44
Facet focal length variants (m)	27, 35, 44, 50, 55
Nominal facet slope error (mrad)	1.4
Nominal tracking error (mrad)	1.0
Nominal facet solar specular reflectivity	0.9
Nominal focal point (m)	(0,0,26.8)
Likely location of sodium receiver aperture centroid	(-2.35, 0.23, 28.03)

Table 1. Key parameters for the 'Solar Field 2' experimental CSP facility.

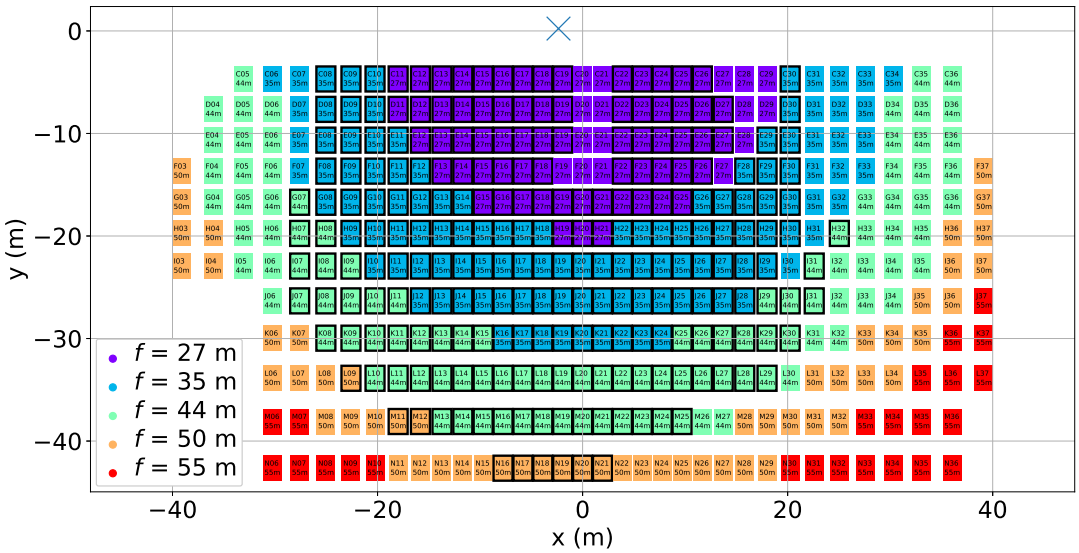

Figure 1. Heliostat seating plan for 'Solar Field 2', with facet focal lengths (f) indicated. Heliostats used for the design point simulations considered in the present work are outlined in black. '×' denotes the likely location of sodium receiver aperture centroid.

3. Receiver design

As visualised in Figure 2, the CSIRO 'Mark I' sodium receiver design is a cavity receiver with a circular aperture. The receiver is mounted on the tower so that the elevation angle of the aperture normal is -52°. Dimensioned drawings are presented in Figure 3. There are two independent flow paths on the east and west sides of the receiver, as illustrated in Figure 4. Each flow path has 3 pipe modules. The inlet of each flow path is at the top of the central pipe modules ('E0' and 'W0'), where the sodium then passes through the modules in a serpentine fashion to exit at the bottom of the outer modules ('E2' and 'W2').

A summary of the key parameters describing the heat transfer pipes is presented in Table 2. The additional strength of Inconel is required for this application due to the combination of high temperature and high flux. The number of pipes per module gradually decreases from the middle to the outer module. This allows more pipes to be placed in the center of the cavity where higher flux can be tolerated due to the lower sodium temperature, and fewer pipes in the sides of the cavity where optical access from the heliostat field is limited.

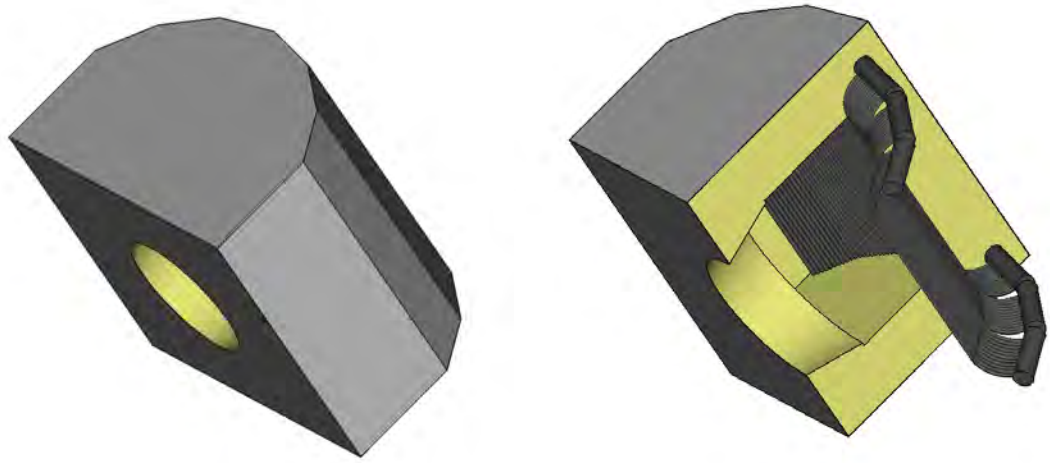

(a) Whole (b) Cutaway of casing and insulation

Figure 2. 3D rendering of the CSIRO 'Mark I' sodium receiver.

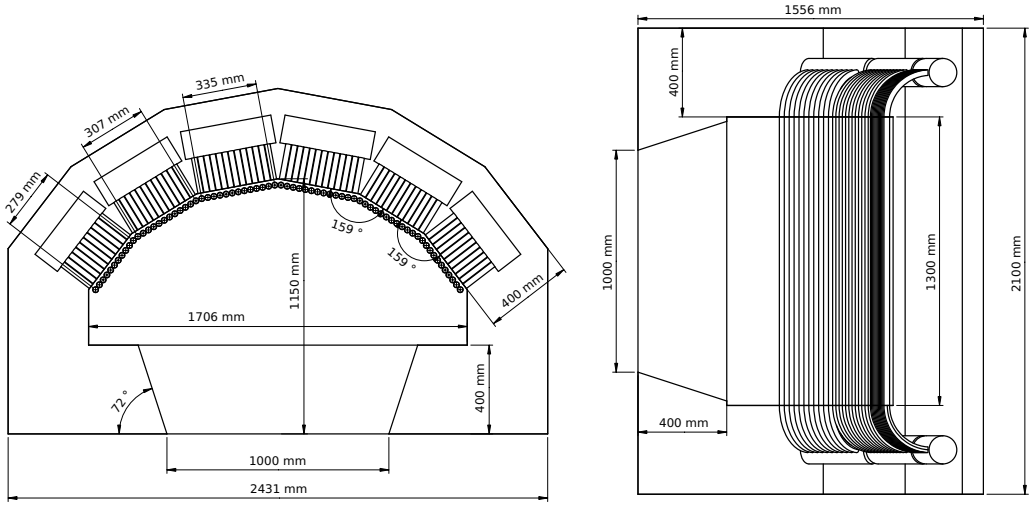

(a) Top cutaway view (b) Side cutaway view

Figure 3. Drawings of the CSIRO 'Mark I' sodium receiver with key dimensions.

4. Physical modelling

4.1. Receiver geometry

Visualisations of the two receiver surface meshes considered in the present work are shown in Figure 5. The simple model approximates the pipe modules as flat surfaces that pass through the pipe centrelines, whilst the detailed model retains the actual geometry of each cylindrical pipe, with the gap between pipes and the backing insulation included. The backing insulation is offset one pipe diameter (25.4 mm) from the pipe centrelines. The detailed model has over 5 times as many triangular facets in the surface mesh. For the simple model, the width discretisation for each of the flat surfaces representing the pipe modules is equal to the number of pipes, so that each pipe can be neatly mapped onto a vertical column of triangular facets. In the detailed model, each pipe is discretised in the circumferential direction by 15 points.

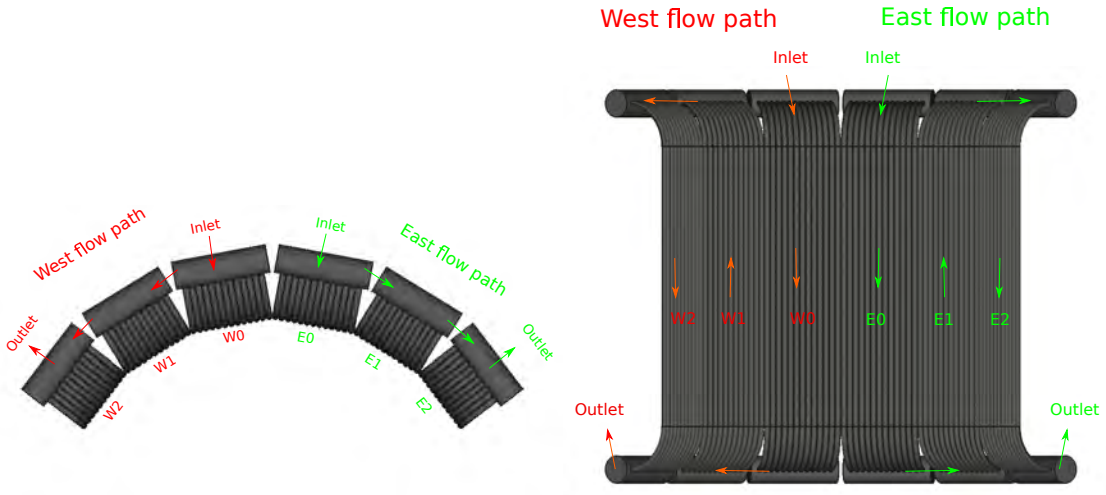

(a) Top view (b) Front view

Figure 4. Diagrams of the flow path arrangement for the CSIRO 'Mark I' sodium receiver.

Parameter	Value
Pipe outer diameter (mm)	25.4
Pipe wall thickness (mm)	1.65
Pipe separation (mm)	2.5
Irradiated length of each pipe (m)	1.6
Pipe material	Seamless Inconel 625
Pipe coating	Pyromark 2500
Pipe count per module (0,1,2)	13, 12, 11

Table 2. Key heat transfer pipe parameters for the CSIRO 'Mark I' sodium receiver..

4.2. Heliostat optics

The Monte Carlo ray tracing model implemented in Heliosim is utilised to simulate the heliostat optics. Rays are cast from the primary reflection surfaces (i.e. heliostat facets). The incident direction (due to sun shape), mirror intercept location and mirror surface normal direction (due to desired facet orientation, tracking error and slope error) for each ray are calculated via Monte Carlo sampling of cumulative distribution functions using the function inversion method. The traversal of rays through the scene (comprised of surface meshes describing the terrian, heliostats, tower and receiver) is performed by the GPU accelerated NVIDIA OptiX Ray Tracing Engine (Parker et al., 2010). The energy partitioning (Modest, 2003) method of accounting for ray reflections is applied, where the energy of each ray is gradually depleted according to the solar absorptance of each surface it interacts with.

The ray tracing parameters for simulating the heliostat optics in the present work are listed in Table 3. Although a statistical tracking error model has been implemented in Heliosim where the heliostat orientation is randomly perturbed about the rotation axes using Monte Carlo sampling, in the present work the slope (1.4 mrad) and tracking error (1.0 mrad) are combined into an effective slope error (1.72 mrad) for consistency with the approach of other groups in the project.

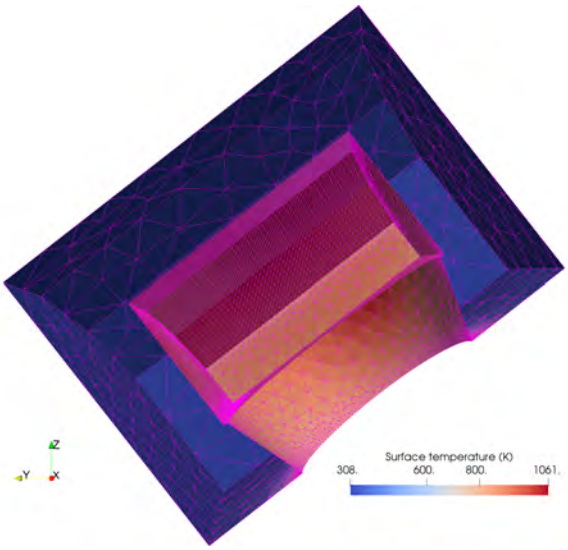

(a) Simple model (13170 triangular facets)

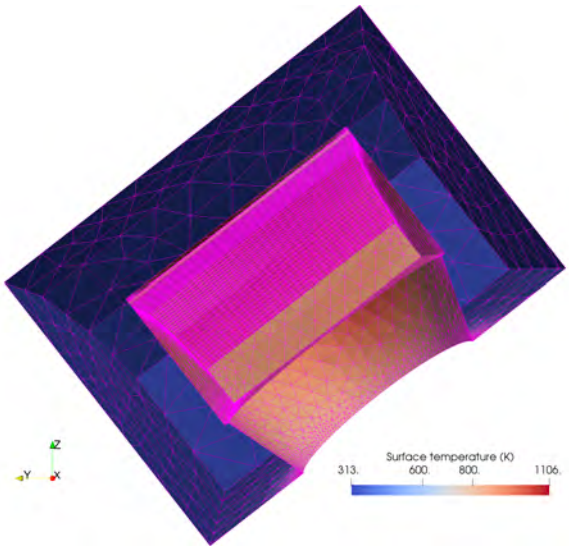

(b) Detailed model (77228 triangular facets)

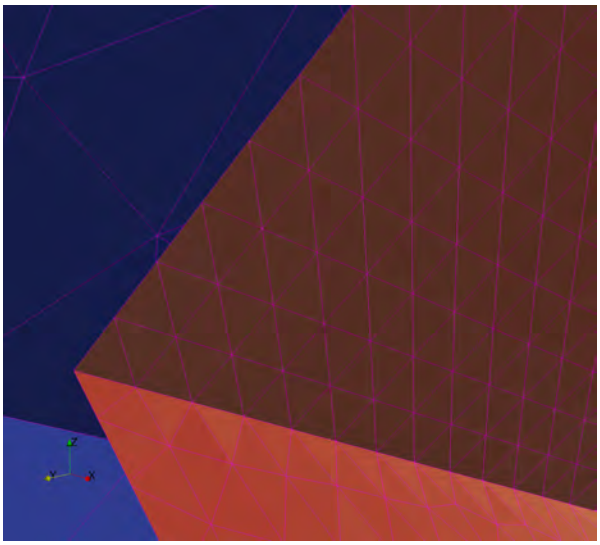

(c) Simple model (close up of 'pipes')

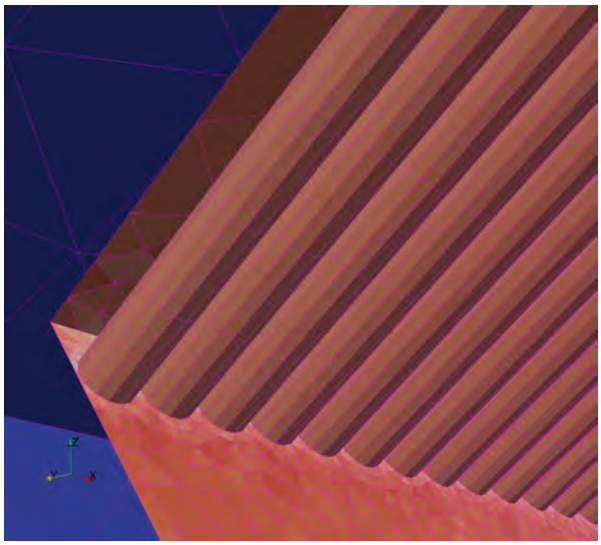

(d) Detailed model (close up of pipes)

Figure 5. Visualisations of the receiver meshes for the simple and detailed models. The meshes have been clipped by the vertical symmetry plane to show the cavity interior.

Parameter	Value
Sun shape	Buie model (Buie et al., 2003)
Circumsolar ratio	0.02
Atmospheric attenuation	DELSOL3 23 km visibility model (Kistler, 1986)
Effective heliostat facet slope error (mrad)	1.72
Rays cast per heliostat (simple, detailed)	10^5, 10^6
Maximum surface interactions per ray	30

Table 3. Parameters for ray tracing simulation of the heliostat optics .

4.3. Receiver heat transfer

Receiver heat transfer is simulated by solving the system of nonlinear equations describing a steady state flux balance for each of the facets in the receiver surface mesh. Illustrations of the facet flux balances for each of the surface types (i.e. insulated wall or heat transfer pipe wall) are presented in Figure 6. The facet view factors required for thermal radiation exchange are calculated using Monte Carlo ray tracing, where 2×10^4 and 4×10^4 rays are cast per facet for the simple and detailed models, respectively. Lateral conduction in walls and circumferential conduction in pipe walls is neglected, on the basis that the temperature gradients in these directions are relatively low. For the simple model the front half of the pipe is assumed to have a uniform surface temperature equal to the corresponding mesh facet, and the rear half of the pipe is considered adiabatic. The area difference between the mesh facet and the section of pipe it represents is taken into account when computing radial conduction in the simple model.

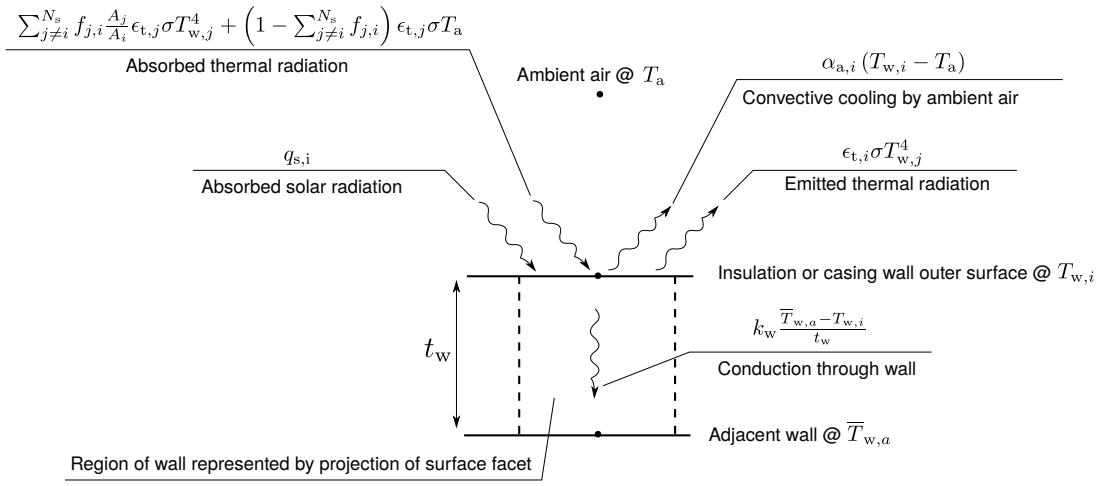

(a) Insulated surfaces

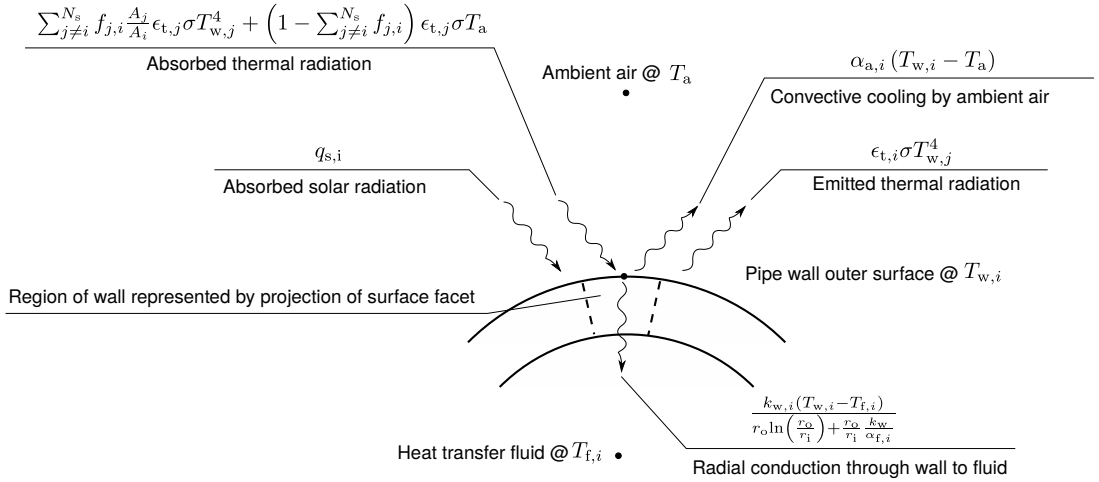

(b) Heat transfer pipe surfaces

Figure 6. Illustration of terms included in the flux balance for each surface mesh facet.

The input parameters for the flux balance equations are listed in Table 4. The fixed ambient convective heat transfer coefficients were conservatively estimated based on empirical correlations and CFD simulations of similar geometries. In the case of the detailed model, the fixed convective heat transfer coefficient of 10 W/m/K is not appropriate for all surfaces inside the

cavity as this value was calculated for a flat surface representation of the pipe modules. The convective heat transfer coefficients for the rear half of the pipes and the insulation behind the pipes and is set to zero, based on the assumption that the flow of ambient air in this region is negligible due to the small gap between pipes. The convective heat transfer coefficient for the front half of the pipes is equal to the 10 W/m/K used in the flat surface model multiplied by a factor of $\frac{2}{\pi}$ to account for the increased surface area compared to a flat surface. A similar approach for utilising convective heat transfer coefficients from correlations developed for flat surfaces was implemented by Cagnoli et al. (2019).

Table 4. Input parameters for the receiver flux balance equations.

Part	Pipes	Insulation	Casing	Shielding[a]
Material	Iconel 625	Isowool Isolite	Zincalume	253MA
Thickness (mm)	1.65	400	2	3
Solar reflectance	0.06	0.7	0.2	0.2
Thermal emittance	0.85	0.5	0.85	0.85
Thermal conductivity (W/m/K)	$5.53 + 1.43 \times 10^{-2}T$ $+4.19 \times 10^{-7}T^2$	0.25	23	23
Ambient convection coefficient (W/m^2/K)	10 (6.37)[b]	10 (0)[c]	20	20

[a] Shielding refers to the steel plate around the aperture
[b] Value in parentheses is for the front half of the cylindrical pipes in the detailed model.
[c] Value in parentheses is for the insulation behind the pipes in the detailed model.

The system of nonlinear equations from the surface mesh flux balance are solved using Newton iterations, where the variable being solved for is the vector of surface temperatures. The Jacobian matrix is analytically estimated, and its inversion is computed by the Armadillo (Sanderson and Curtin, 2016) linear algebra library. For a given vector of surface temperatures, the sodium flow state along each pipe is calculated by solving the mass, momentum and energy conservation equations for plug flow. The thermodynamic and transport properties of sodium are taken from Boerema et al. (2012), and the Nusselt number is evaluated at the film temperature using the uniform flux correlation proposed by Sleicher and Rouse (1975). The total mass flow rate of sodium in each flow path is iterated until the desired outlet temperature of 740 °C is achieved to within ± 1°C.

5. Results

Simulations were performed for both the simple and detailed models at the Equinox design point conditions, Table 5. 239 heliostats (as indicated in Figure 1) were utilised, allowing the receiver to slightly exceed the 700 kW thermal power capacity it was design for. These heliostats were selected to maximise interception efficiency, whilst taking into account the shadow cast by the tower on the field. The resulting solar flux distribution on the pipe modules is shown in Figure 7, and a summary of the key performance parameters is given in Table 6. A comparison of the net flux and sodium temperature profiles along the eastern flow path is presented in Figure 8.

Parameter	Value
Solar elevation angle (°)	56.9
Solar azimuth angle (°)	0
Direct normal irradiance (W/m^2)	900
Ambient temperature (°C)	25

Table 5. Design point solar and ambient conditions.

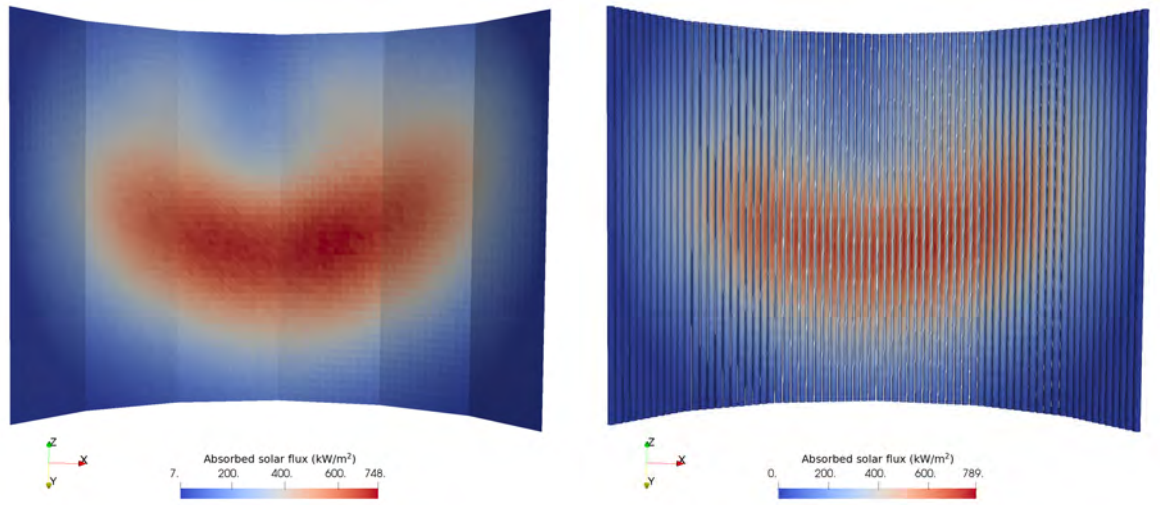

(a) Simple model **(b) Detailed model**

Figure 7. Distrbution of solar flux on the pipe modules from the design point simulations.

Parameter	Value	
Model	Simple	Detailed
Power through aperture (kW)	798.9	798.4
Spillage loss (kW)	26.0	26.1
Receiver solar reflection loss (kW)	14.9	13.1
Receiver thermal radiation loss (kW)	28.9	27.2
Receiver convection loss (kW)	47.9	45.8
Receiver conduction loss (kW)	5.2	6.7
HTF thermal output (kw)	702.0	705.6
Aperture interception efficiency (%)	96.84	96.83
Receiver efficiency (%)	87.88	88.37
Combined interception and receiver efficiency (%)	85.10	85.57
East flow path average mass flow rate per pipe (kg/s)	0.100	0.100
West flow path average mass flow rate per pipe (kg/s)	0.112	0.113
East flow path peak net flux (kW/m^2)	706.0	721.7
West flow path peak net flux (kW/m^2)	728.6	753.2

Table 6. Summary of results for design point simulations.

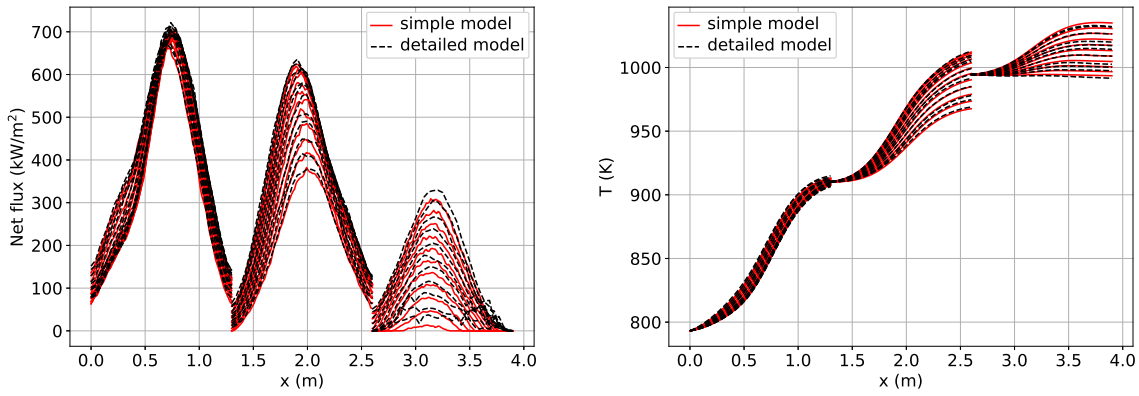

(a) Net flux **(b) Sodium temperature**

Figure 8. Comparison of eastern flow path profiles for the simple and detailed model. Net flux is the heat conducted radially through the pipe wall to the fluid. For the detailed model, the maximum net flux is used for axial location.

6. Discussion

6.1. Thermal power output

The thermal power output predicted by the simple model is 0.5 % lower than the detailed model. The breakdown of thermal losses in Table 6 is instructive in understanding the cause of this difference. The simple model over predicts solar radiation, thermal radiation and convection losses. The over prediction of radiative losses by the simple model may be due to the enhanced 'light trapping' ability of a rough surface relative to a smooth surface (Ho et al., 2016). The over prediction of convection losses is due to the simple model not considering the gap between pipes.

6.2. Net flux

The simple model under predicts the maximum net flux at the pipe outer wall by up to 3.3 % relative to the detailed model. The largest difference in net flux is in the outer module, where the simple model result is up to 7 % lower (see Figure 8a). Accurately predicting the net flux through the pipe wall is important for determining the thermally induced stress in the pipe walls. Circumferential flux distributions for the middle-most pipes of the modules in the eastern flow path are presented in Figure 9. While the net and absorbed solar flux for the central module ('E0') approximately follows a cosine distribution as expected for normal incident irradiance, the middle ('E1') and outer ('E2') modules deviate from this symmetric distribution. This is due to the pipe modules not being exactly radially orientated relative to the aperture centroid. Although such a radial orientation would make more efficient use of the pipe surface for capturing incident radiation (pipe-to-pipe shading would be avoided), this was found during the receiver design process to result in a receiver that was either too large or had pipes too close to the aperture resulting in excessive peak net flux.

Figure 9a shows that the assumption made in the simple model of an adiabatic pipe rear is incorrect. This is due to considerable levels of radiation passing through the gaps between pipes (gaps are 10 % of pipe outer diameter) and irradiating the backing insulation, a fraction of which is absorbed by the rear of the pipes in the form of reflected solar radiation (Figure 9b)

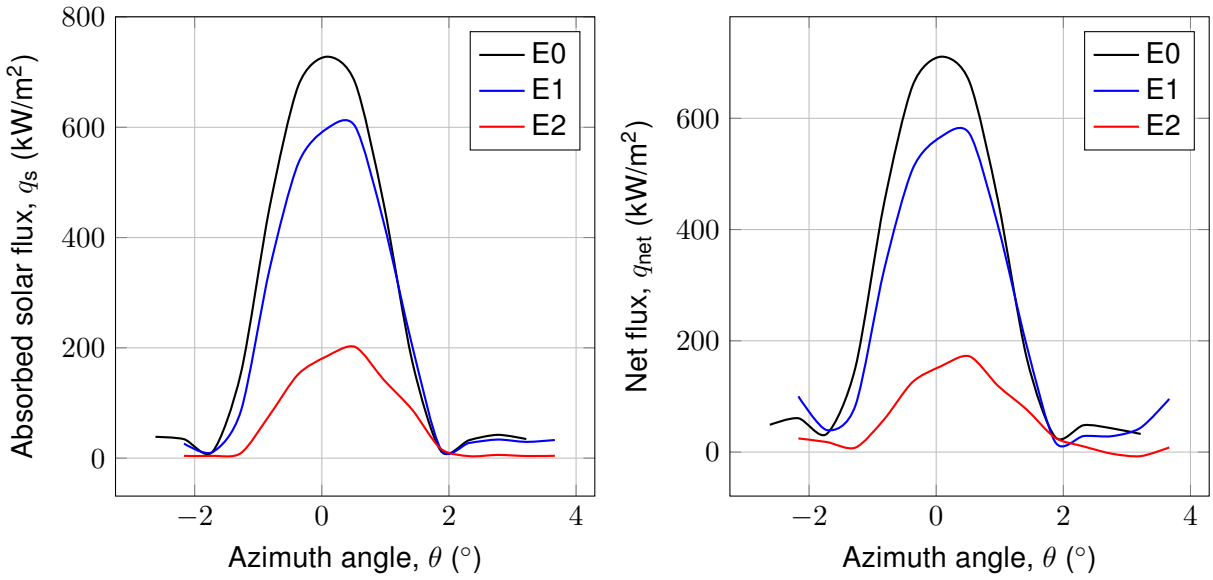

(a) Absorbed solar flux **(b) Net flux through outer wall**

Figure 9. Circumferential distributions for the middle-most pipes of the modules in the eastern flow path.

and re-emitted thermal radiation.

6.3. Grid resolution

A number of grid resolutions were assessed for the detailed model. The wall time, peak memory usage and calculated thermal output for each, along with that for the simple model for reference, are plotted in Figure 10. The ray tracing and receiver heat transfer simulations were performed on different computers, due to their specific hardware requirements (i.e. a GPU for ray tracing and a large amount of memory for heat transfer). The ray tracing simulations were performed using an NVIDIA Quadro M2000M GPU, and the receiver heat transfer simulations on a Dell PowerEdge M630 server with dual 10 core Intel Xeon E5-2660 V3 processors and 512 GB of memory. The simple model required only 10 minutes and 10.4 GB of memory, whilst the detailed required up to 30 hours and 215 GB of memory. Wall time and memory usage have approximately first and second-order dependence on the number of cells. This is due to the most resource intensive part of the simulation being the Jacobian matrix inversion from the heat transfer simulation, where the number of elements in the matrix is equal to the square of the cell count. Although the thermal power output predicted by the three grid resolutions considered for the detailed model vary by only 0.03 %, the result does not converge as the number of cells is increases. This is most likely due to random variation associated with the Monte Carlo ray tracing model, indicating the ray resolution may not have been high enough for the high resolution meshes.

7. Conclusion

This work has demonstrated the importance of considering the actual cylindrical geometry of heat transfer pipes when simulating tubular receivers. This is especially relevant to the design of cavity receivers for high temperature HTFs where the incident irradiance is not always normal to the pipe crown. The detailed model implemented in the present work, however, requires

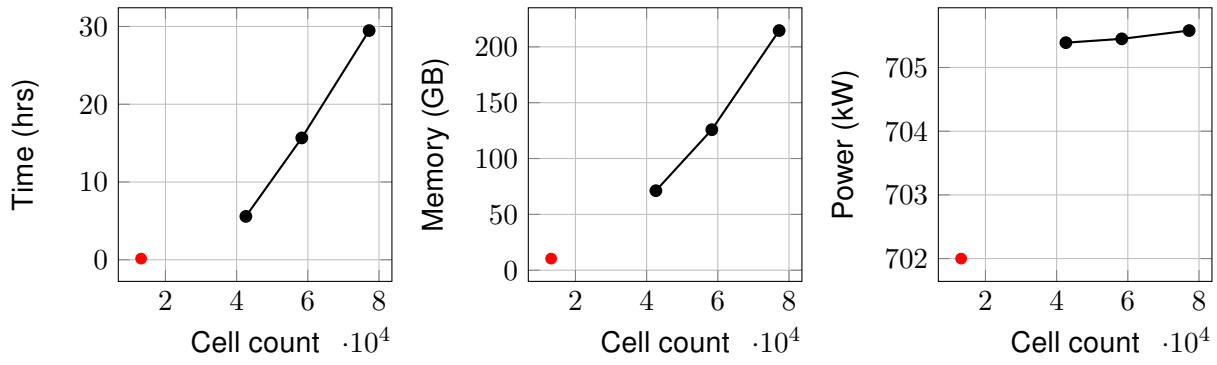

(a) Wall time **(b) Peak memory usage** **(c) Calculated thermal output**

Figure 10. Resource usage and calculated result as a function of cell count in the receiver mesh for the simple model (•) and detailed model (—●—).

considerable computational resources and is not appropriate for iterative optimisation methods where many objective function evaluations are required. The main computational bottleneck for the detailed model is the inversion of the Jacobian matrix when solving the facet flux balance equations. Alternative formulations and solution methods for the receiver heat transfer equations may allow for both increased accuracy and reduced computational requirements. Possibilities include:

1. Encoding a more accurate estimation of the Jacobian matrix so that the number of iterations (and therefore wall time) to convergence is reduced,
2. Using a Jacobian-free nonlinear solver such as the Newton-Krylov method to significantly reduce the memory requirement, or
3. Simulating the complete conjugate heating problem with a finite volume framework such as OpenFOAM.

In lieu of these more advanced implementations, the simple and detailed models presented in this work can be used in conjunction with one other to design tubular receivers with both reasonable accuracy and computational efficiency.

Acknowledgements

The Australian Solar Thermal Research Institute (ASTRI) program is supported by the Australian Government, through the Australian Renewable Energy Agency (ARENA).

References

Boerema, N., G. Morrison, R. Taylor, and G. Rosengarten (2012, sep). Liquid sodium versus Hitec as a heat transfer fluid in solar thermal central receiver systems. *Solar Energy 86*(9), 2293–2305.

Buie, D., A. G. Monger, and C. J. Dey (2003). Sunshape distributions for terrestrial solar simulations. *Solar Energy 74*(March 2003), 113–122.

Burton, A. I. and G. Andrews (2011). *Australian Patent No. AU 2011349053.* Retrived from http://pericles.ipaustralia.gov.au/ols/auspat/applicationDetails.do?applicationNo=2011349053.

Cagnoli, M., A. de la Calle, J. Pye, L. Savoldi, and R. Zanino (2019, jan). A CFD-supported dynamic system-level model of a sodium-cooled billboard-type receiver for central tower CSP applications. *Solar Energy 177*, 576–594.

Ho, C. K., J. M. Christian, J. Yellowhair, J. Ortega, and C. Andraka (2016, may). Fractal-like receiver geometries and features for increased light trapping and thermal efficiency. In *AIP Conference Proceedings*, Volume 1734, pp. 030021. AIP Publishing LLC.

Kistler, B. L. (1986). A user's manual for DELSOL3: A computer code for calculating the optical performance and optimal system design for solar thermal central receiver plants. Technical report, Sandia National Laboratories, Albuquerque, NM, SAND86-8018.

Modest, M. F. (2003). The Monte Carlo Method for Thermal Radiation. *Radiative HeatTransfer*, 644–679.

Padilla, R. V., Y. C. Soo Too, R. Benito, and W. Stein (2015, jun). Exergetic analysis of supercritical CO2 Brayton cycles integrated with solar central receivers. *Applied Energy 148*, 348–365.

Parker, S. G., J. Bigler, A. Dietrich, H. Friedrich, J. Hoberock, D. Luebke, D. McAllister, M. McGuire, K. Morley, A. Robison, and M. Stich (2010). OptiX: A general purpose ray tracing engine. *ACM Transactions on Graphics 29*(4), 10.

Potter, D., A. Burton, and J.-s. Kim (2015). Optimised Design of a 1 MWt Liquid Sodium Central Receiver System. In R. Egan and R. Passey (Eds.), *Proceedings of the Asia Pacific Solar Research Conference*, pp. 10. Australian PV Institute.

Potter, D. F., J.-S. Kim, A. Khassapov, R. Pascual, L. Hetherton, and Z. Zhang (2018). Heliosim: an integrated model for the optimisation and simulation of central receiver CSP facilities. In *AIP Conference Proceedings*, Volume 2033, pp. 210011. AIP Publishing LLC.

Romero, M. and J. González-Aguilar (2017, jan). Next generation of liquid metal and other high-performance receiver designs for concentrating solar thermal (CST) central tower systems. *Advances in Concentrating Solar Thermal Research and Technology*, 129–154.

Sanderson, C. and R. Curtin (2016). Armadillo: a template-based C++ library for linear algebra. *The Journal of Open Source Software 1*(2), 26.

Schiel, W. J. and M. A. Geyer (1988, jan). Testing an external sodium receiver up to heat fluxes of 2.5 MW/m2: Results and conclusions from the IEA-SSPS high flux experiment conducted at the central receiver system of the Plataforma Solar de Almeria (Spain). *Solar Energy 41*(3), 255–265.

Sleicher, C. and M. Rouse (1975, may). A convenient correlation for heat transfer to constant and variable property fluids in turbulent pipe flow. *International Journal of Heat and Mass Transfer 18*(5), 677–683.

Wang, Y., D. Potter, C.-A. Asselineau, C. Corsi, M. Wagner, M. Blanco, J.-S. Kim, and J. Pye (2018, nov). Comparison of optical modelling tools for sunshape and surface slope error. In *AIP Conference Proceedings*, Volume 2033, pp. 210020. AIP Publishing LLC.